Metal-insulator transition in $Ba_3Fe_{1-x}Ru_{2+x}O_9$: Interplay between site disorder, chemical percolation, and electronic structure

S. Middey,[1,2] Payel Aich,[3] C. Meneghini,[4] K. Mukherjee,[5] E. V. Sampathkumaran,[5] V. Siruguri,[6] P. Mahadevan,[7] and Sugata Ray[1,3,*]

[1]*Centre for Advanced Materials, Indian Association for the Cultivation of Science, Jadavpur, Kolkata 700032, India*
[2]*Department of Physics, University of Arkansas, Fayetteville, Arkansas 72701, USA*
[3]*Department of Materials Science, Indian Association for the Cultivation of Science, Jadavpur, Kolkata 700032, India*
[4]*Science Department, University Roma Tre, Via della vasca navale 84, I-00146 Rome, Italy*
[5]*Tata Institute of Fundamental Research, Homi Bhabha Road, Colaba, Mumbai 400005, India*
[6]*UGC-DAE Consortium for Scientific Research Mumbai Centre, R5 Shed, Bhabha Atomic Research Centre, Mumbai 400085, India*
[7]*S. N. Bose National Centre for Basic Sciences, JD-Block, Sector III, Salt Lake, Kolkata 700098, India*

(Received 1 August 2016; revised manuscript received 22 September 2016; published 18 November 2016)

Perovskites containing barium metal at the A site often take up unusual hexagonal structures having more than one type of possible sites for the B cation to occupy. This opens up various different B-B- or B-O-B-type connectivities and consequent physical properties which are naturally missing in cubic perovskites. $BaRuO_3$ is one such system where doping of Ru ($4d^4$) by other transition metals (M^{n+}) creates similar conditions, giving rise to various M-Ru interactions. Interestingly, the $6H$ hexagonal structure of doped barium ruthenate triple perovskite ($Ba_3MRu_2O_9$) seems to possess some internal checks because within the structure M ion always occupies the $2a$ site and Ru goes to the $4f$ site, allowing only M-O-Ru 180° and Ru-O-Ru 90° interactions to occur. The only exception is observed in the case of the Fe dopant, which allows us to study almost the full $Ba_3Fe_{1-x}Ru_{2+x}O_9$ series of compounds with wide ranges of x because here Fe ions have the ability to freely go to the $4f$ sites and Ru readily takes up the $2a$ positions. Therefore, here one has the opportunity to probe the evolution of electronic and magnetic properties as a function of doping by going from $BaRuO_3$ (paramagnetic metal) to $BaFeO_3$ (ferromagnetic insulator). Our detailed experimental and theoretical results show that the series does exhibit a percolative metal-insulator transition with an accompanying but not coincidental magnetic transition as a function of x.

DOI: 10.1103/PhysRevB.94.184424

I. INTRODUCTION

Chemical doping in complex oxides results in diverse phenomena, including metal-insulator transition, colossal magnetoresistance, high-temperature superconductivity, charge ordering, orbital ordering, etc. [1–3]. The intrinsic chemical disorder, introduced by doping, may also have a significant effect on the resulting behavior of the system [4]. However, the microscopic impact of such disorders often remains unnoticed in standard diffraction experiments, which look for only an average unit cell. Therefore, the necessity of advanced microscopic probes becomes paramount [5–7].

$Ba_3FeRu_2O_9$, a $\frac{1}{3}$ Fe-doped $BaRuO_3$ perovskite, is an apparently simple compound with a standard $6H$ hexagonal structure [Fig. 1(a)]. However, $Ba_3FeRu_2O_9$ possesses a special property of placing Fe and Ru randomly in all the octahedral sites [8,9], while for almost all other members of the $Ba_3MRu_2O_9$ family, M (M = transition-metal, rare-earth ion) always occupies the $2a$ site and Ru exclusively occupies both the $4f$ sites (see the $6H$ structure in Fig. 1(a) for site identification) [8,10–14]. Interestingly, this characteristic makes the situation far more complex than what just a conventional site-disordered unit cell with consistent chemical composition (maintaining the overall formula $Ba_3FeRu_2O_9$ for each cell) can describe. Here significant microscopic phase separation is observed with complementary Fe-rich and Ru-rich small regions [9], where the chemical formulaic sanctity within a unit cell is not maintained and which can be established only by considering a fairly large sample volume. As a result, the electronic and magnetic properties of $Ba_3FeRu_2O_9$ warranted a different discussion based primarily on their microscopic phase division [9].

The other consequence of the above-mentioned Fe/Ru site flexibility is the ease of achieving a wide range of Fe-doped $BaRuO_3$ compounds maintaining the structure at ambient conditions, so that one is not restricted to a rigid $Ba_3MRu_2O_9$ formula, where M refuses ever to occupy $4f$ sites and consistently occupies only the $2a$ site. Accordingly, in this paper we report detailed experimental results from a $Ba_3Fe_{1-x}Ru_{2+x}O_9$ series of systems with $-1.0 \leqslant x \leqslant 0.35$, synthesized under ambient pressure. This series becomes a curious case because, electronically, the two end members, i.e., $BaRuO_3$ ($x = 1$, nine-layered hexagonal, paramagnetic metal [15]) and $BaFeO_3$ ($x = -2$, cubic, ferromagnetic metal [16] or insulator [17]; never achieved under ambient conditions), are quite different, and therefore, the series is expected to exhibit magnetic and/or electronic transitions as a function of x, but the additional effect of Fe/Ru disorder within an altered $6H$ structure can hardly be anticipated.

To address this issue, we have carried out a series of experiments on $Ba_3Fe_{1-x}Ru_{2+x}O_9$ compounds and found a composition-dependent insulator-metal transition, where the signature of inhomogeneous magnetism is not only retained throughout but also evolved as a function of x. Our extended x-ray absorption fine-structure (EXAFS) analysis suggested

*Corresponding author: mssr@iacs.res.in

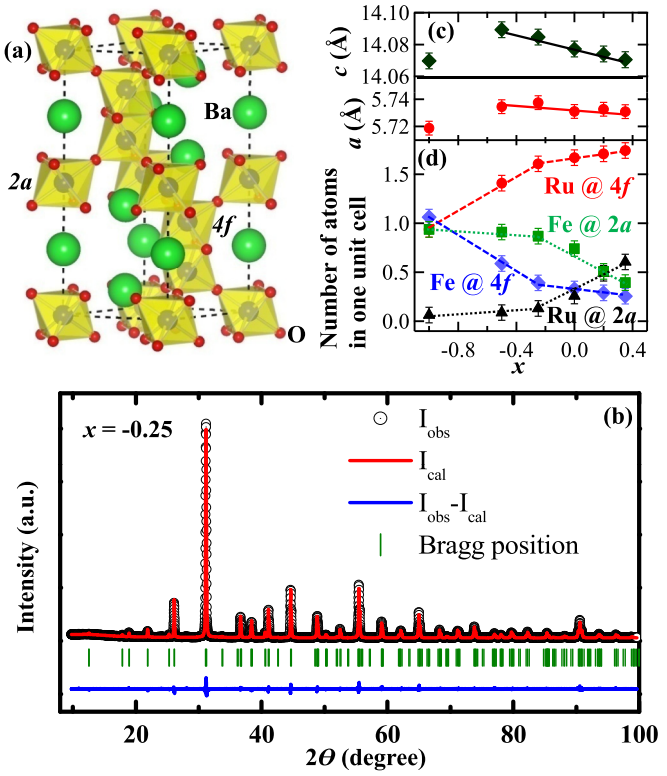

FIG. 1. (a) Crystal structure of $Ba_3MRu_2O_9$. (b) Experimental (black) and refined (red) XRD patterns for $x = -0.25$ at room temperature. The blue line represents the difference between the observed and calculated patterns, and the Bragg positions are marked as vertical green lines. Variation of (c) lattice constants and (d) Fe and Ru occupancies at the $2a$ and $4f$ sites with doping x along with the error bars. The data for the parent compound are adapted from Ref. [9].

that each of the members developed its own microscopic Fe- and Ru-rich regions, the spread and volume fraction of which depended closely on the nominal x. We found that the evolution of phase separation is such that the higher-Fe-containing compounds ($x < 0$) started to order magnetically at higher temperatures and also became insulating, while just the opposite happened in compounds having large Ru content ($x > 0$). Needless to say, homogeneous changes in the relative ratio of Fe and Ru are expected to affect both the magnetic and electronic properties independent of the aforesaid phase separation, but our results suggest that the main effect indeed appears because of the microscopic inhomogeneity, and as a result, percolative effects take over the electronic effects.

II. EXPERIMENTAL DETAILS

Polycrystalline samples with the general formula $Ba_3Fe_{1-x}Ru_{2+x}O_9$, with $x = -1.0$, -0.5, -0.25, 0.0, 0.1, 0.2, 0.35, have been synthesized by conventional solid-state synthesis [9]. Powder x-ray diffraction (XRD) patterns, recorded by a Bruker AXS: D8 Advanced x-ray diffractometer equipped with Cu K_α radiation, were refined using the Rietveld method using the FULLPROF [18] program. Fe K-edge EXAFS spectra were collected at the XAFS beamline of the Elettra Synchrotron center in Italy [19]. Transport properties were measured by standard four-probe methods. The magnetic properties were studied in a Quantum Design superconducting quantum interference device magnetometer. The heat capacity was measured using the relaxation method in a Quantum Design Physical Property Measurement System. Ultraviolet photoelectron spectroscopy (UPS) was used to determine the valence-band density of states. Spectra were collected in an Omicron electron spectrometer equipped with an EA125 analyzer and high-intensity VUV source HIS 13.

III. RESULTS AND DISCUSSION

Powder XRD data collected for the sample with $x = -0.25$ from several members of the $Ba_3Fe_{1-x}Ru_{2+x}O_9$ series are shown in Fig. 1(b), which confirms complete phase purity except for the sample with $x = 0.35$, which has some tiny impurity peaks, the strongest of which is indicated by an asterisk (see Fig. S1 in the Supplemental Material [20]). This extra peak is likely due to the development of some four-layered hexagonal phase. With further increase in x, the intensity of this extra peak increases, and hence, only the samples with $x \leqslant 0.35$ will be discussed here. For other samples, all peaks in the XRD pattern could be satisfactorily indexed and refined (red curve) with the six-layered hexagonal ($6H$) crystal structure with space group $P6_3/mmc$. Ru and Fe occupancies at the $2a$ (Q site) and $4f$ (P site) positions were jointly varied with the constraint that the total atomic count remained in synergy with the chemical formula unit. The refined structural parameters are listed in Table I.

The lattice constants a and c, obtained from the refinement, tend to decrease with an increase in Ru concentration [Fig. 1(c)] except for the extreme end member with $x = -1.0$. This observation appears to be opposite the expected behavior from Vegard's law [21] as the average Shannon radii [22] increase with x [23]. This apparent deviation is likely to be associated with the change of Ru-Ru separation within the Ru_2O_9 dimer ($4f$ sites) with the change in the average oxidation state of Ru [24]. As the average valency of Ru in $Ba_3Fe_{1-x}Ru_{2+x}O_9$ decreases with replacement of Fe by Ru, the effective Coulomb repulsion within the dimer decreases, resulting in an overall decrease in lattice constants [24,25]. The importance of the aforementioned cation-cation repulsion is also apparent from the off-center displacements of the Ru ions Δ, defined as the displacement of the cation located at the $4f$ site [P site, Fig. 1(a)] from the ideal position $(1/3, 2/3, 1/6)$ [25]. Clearly, Δ (see Table 1) tends to decrease with increasing x, justifying the seemingly "ambiguous" lattice-parameter variation. The decrease in a and c for $x = -1.0$ could also be at least partially related to the nonstoichiometry in oxygen content. The number of Fe and Ru atoms sitting at $2a$ and $4f$ sites in one formula unit (obtained from refinement) is plotted as a function of x in Fig. 1(d). For the most Ru deficient sample ($x = -1.0$), almost all the Ru atoms are found to occupy the face-shared octahedral sites, indicating an inherent preference of Ru for the P sites (the overwhelmingly significant preference dominating most other $Ba_3MRu_2O_9$ members). However, for $x > -0.25$ Ru tends to occupy the $2a$ site (Q site) too, presenting the curious case of these Fe-doped $6H$ $BaRuO_3$ compounds under ambient conditions.

TABLE I. Structural parameters for $Ba_3Fe_{1-x}Ru_{2+x}O_9$. The atomic positions are Ba(1), $2b(0, 0, 1/4)$; Ba(2), $4f(1/3, 2/3, z)$; Ru/Fe, $4f(1/3, 2/3, z)$; Fe/Ru, $2a(0, 0, 0)$; O(1), $6h(x, 2x, 1/4)$; O(2), $12k(x, 2x, z)$. The structural data for $x = 0.0$ were reported in Ref. [9]. The constrained parameter is $B_{Ba(1)} = B_{Ba(2)}$.

	x					
	−1.0	−0.5	−0.25	0.0	0.2	0.35
$a \pm 0.005$ (Å)	5.719	5.734	5.737	5.731	5.733	5.731
$c \pm 0.005$ (Å)	14.070	14.089	14.085	14.077	14.074	14.070
Ba1: B (Å^2)	0.382(4)	0.132(6)	0.228(7)	0.505(3)	0.380(2)	0.359(6)
Ba2: z	0.910(1)	0.908(2)	0.908(8)	0.909(2)	0.909(1)	0.909(3)
Ba2: B (Å^2)	0.382(4)	0.132(6)	0.228(7)	0.505(3)	0.380(2)	0.359(5)
Ru/Fe (P site): z	0.152(3)	0.154(7)	0.155(7)	0.156(6)	0.156(6)	0.157(1)
Ru/Fe (P site): B (Å^2)	0.386(7)	0.099(8)	0.441(7)	0.347(4)	0.583(2)	0.633(8)
Ru/Fe (P site): $n \pm 0.07$	0.47/0.53	0.71/0.29	0.80/0.20	0.83/0.17	0.85/0.15	0.87/0.13
Ru/Fe (Q site): B (Å^2)	0.603(8)	0.205(8)	0.348(1)	0.347(4)	0.419(9)	0.416(6)
Ru/Fe (Q site): $n \pm 0.07$	0.06/0.94	0.09/0.91	0.13/0.87	0.26/0.74	0.49/0.51	0.61/0.39
O(1): x	0.482(6)	0.492(6)	0.493(9)	0.508(1)	0.488(3)	0.493(2)
O(1): B (Å^2)	0.832(7)	0.452(4)	0.456(6)	0.434(3)	0.456(7)	0.456(6)
O(2): x	0.168(2)	0.166(2)	0.164(3)	0.16(3)	0.175(3)	0.175(4)
O(2): z	0.417(7)	0.418(3)	0.418(7)	0.418(9)	0.419(5)	0.421(2)
O(2): B (Å^2)	0.832(7)	0.486(3)	0.457(3)	0.434(3)	0.457(3)	0.456(6)
R_p (%)	12.2	13.5	12.4	9.98	13.2	16.2
R_{wp} (%)	12.3	11.5	10.8	15.35	12.1	15.3
χ^2	9.2	4.2	4.0	1.26	7.75	6.2

In order to find out the difference between the long range and local structure of these compounds, we also performed Fe K-edge EXAFS measurements which are analyzed following the procedure described earlier [9]. Fe K-edge x-ray absorption spectra (XAS) were collected in transmission mode at room temperature using gas-filled ionization chambers to measure incident (I_o) and transmitted (I_t) x-ray intensities. The x-ray beam energy calibration was monitored during data collection measuring the absorption signal (I_2) of a Fe reference foil placed after the sample. Up to six spectra were measured and averaged to improve the data statistics, resulting in good-quality EXAFS spectra, and were refined in the ∼3–15 Å^{-1} k range. The raw XAS spectra were treated using standard procedures for background subtraction, normalization, edge energy definition, and extraction of the structural EXAFS signal [26]. A first look at the Fe K-edge x-ray absorption near-edge structure (XANES) region is useful to check the average Fe valence state; the XANES of $x = -1.0$, -0.5, 0.2, 0.35 (Fig. S2) appear to be very similar, and more importantly, the edge energy is the same for all the spectra, demonstrating the average Fe^{3+} state is preserved in the whole Fe concentration range. Quantitative analysis of the EXAFS region was carried out using the FITEXA program [26] following the multishell least-squares refinement procedure described earlier [9].

The model curves were calculated as the sum of partial contributions selected from model atomic clusters around the absorber using the standard EXAFS formula and Gaussian disorder approximation [27]; the photoelectron mean free path and scattering amplitude and phase functions were calculated using the FEFF [27] program. The crystallographic data were used to build atomic clusters around Fe in P ($4f$) and Q ($2a$) sites; the main atomic configurations contributing to the EXAFS signal were selected according to their average amplitude, and the relevance to the fitting has been statistically checked [26]. We found the main contributions required to reproduce the experimental data up to about 4–5 Å [Figs. 2(c) and 2(d)] are the Fe-O nearest-neighbor shell, the Fe-Fe/Ru contributions coming from atoms located on the P-P sites of face-sharing octahedra, the Fe-Ba shell, and the Fe-O-Fe/Ru contributions coming from atoms located on the P and Q sites of corner-linked octahedra.

In order to reduce the correlation among best-fit parameters and improve the quality and reliability of the refinement, physical constraints were imposed. In particular, the Fe-O coordination number was fixed to 6, refining the Fe-O distance and disorder factor [mean-square relative displacement (MSRD)]. For the Fe-Fe/Ru contributions the same distance and MSRD were used for Fe-Fe and Fe-Ru; moreover, to constrain their multiplicity [28] numbers N we proceeded by noticing that each Fe on a P site has only one P neighbor site that can be occupied by Fe or Ru, indicating with Y_P (Y_Q) the Fe occupancy of the P (Q) site obtained by XRD data (Table I). The probability to find a Fe ion on a P site is $X = 2Y_P/(2Y_P + Y_Q)$. In the case of a random distribution of Fe and Ru on P sites, the probability that an Fe ion on a P site has an Fe (Ru) ion on the close P site is X $(1 - X)$, so that the fraction of Fe-Fe neighbors, expected on the basis of XRD data, is $M_{FeFe} = X\ Y_P$, and that of Fe-Ru is $M_{FeRu} = X\ (1 - Y_P)$ (Table II). In the preliminary analysis we fixed the multiplicity number of the partial contributions to M_{FeFe} and M_{FeRu}. However, the best fit refines the multiplicity of Fe-Fe and Fe-Ru contributions. In order to be coherent with XRD data we fixed the total

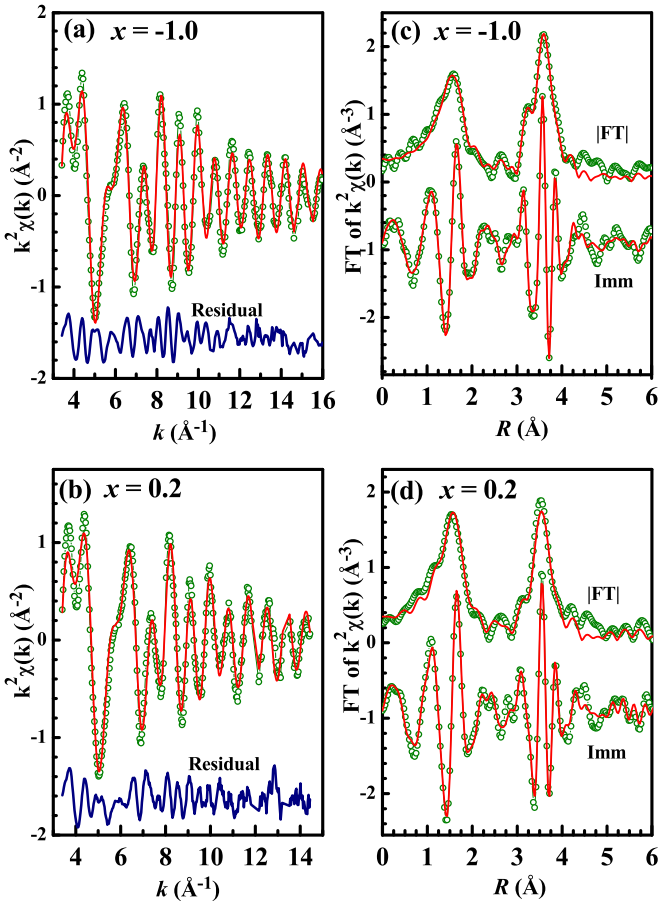

FIG. 2. Fe K-edge EXAFS fitting results. Left: experimental data (points) and best fit are shown in k space for (a) $x = -1.0$ and (b) $x = 0.2$. The residual $k^2\chi_{\text{exp}} - k^2\chi_{\text{th}}$ is shown, vertically shifted for clarity. Right: the moduli and imaginary parts (vertically shifted) of Fourier transforms of experimental (points) and theoretical (lines) EXAFS data for (c) $x = -1.0$ and (d) $x = 0.2$.

Fe-Fe/Ru coordination number $X = (M_{FeFe} + M_{FeRu})$ and refined a free parameter x_{FeFe} to obtain $N_{FeFe} = X\ (x_{FeFe})$ and $N_{FeRu} = X\ (1 - x_{FeFe})$. The third main coordination shell around an Fe absorber is made by Ba ions located around 3.5 Å, but Fe on a P site has 7 Ba neighbors, while Fe on a Q site has 8 Ba neighbors; we used a single contribution and fixed the multiplicity number to $N_{FeBa} = 7X + 8(1 - X)$. The last relevant contribution originates from Fe-O-Fe/Ru configurations and includes single- (SS: Fe $\rightleftharpoons$ Fe/Ru) and multiple-scattering (MS: double and triple scattering, Fe $\rightleftharpoons$ O $\rightleftharpoons$ Fe/Ru) terms enhanced by collinear disposition (focusing effect). We fixed the geometry of Fe-O-Fe/Ru atoms to have the same path length for SS and MS terms (corresponding to perfectly aligned atoms) and $R_{FeOFe} = R_{FeORu}$. To constrain the multiplicities of FeOFe and FeORu contributions we notice that they may originate from an Fe absorber on a P site, in which case it has three Fe/Ru neighbors on a Q site, or an Fe absorber on a Q site, in which case it has six Fe/Ru neighbors on a P site. For a random Fe/Ru distribution we expect $M_{FeOFe} = 3X(Y_Q) + 6(1 - X)Y_P$ and $M_{FeORu} = 3X(1 - Y_Q) + 6(1 - X)(1 - Y_P)$. The best fit is obtained by fixing the sum $K = M_{FeOFe} + M_{FeORu} = 6 - 3X$ but refining a single free parameter y_{FeOFe} to obtain the multiplicities of FeOFe ($N_{FeOFe} = K\ y_{FeOFe}$) and FeORu [$N_{FeORu} = K(1 - y_{FeOFe})$] SS and MS contributions.

TABLE II. Structural results obtained from the refinement of the Fe K-edge XAFS spectrum. Standard uncertainty on the last digit is reported in parentheses for free parameters, and the asterisk indicates fixed or constrained parameters (see discussion). The multiplicity numbers of Fe(Ru) and Fe-O-Fe(Ru) reported within square brackets are calculated using the information for Fe/Ru occupancies at P and Q sites obtained from XRD (see discussion).

	Fe_2Ru		$Fe_{0.8}Ru_{2.2}$	
Shell	N	R (Å)	N	R (Å)
FeO	6*	2.01(1)	6*	2.00(1)
FeFe	0.45(5) [0.28]	2.54(2)	0.38(4) [0.06]	2.52(2)
FeRu	0.05* [0.25]	2.54*	0.0* [0.31]	2.52*
FeBa	7.5*	3.55(2)	7.5*	3.53(2)
FeOFe	2.8(2) [3.0]	3.94(2)	2.3(2) [1.1]	3.97(2)
FeORu	1.6* [1.4]	3.94*	2.5* [3.7]	3.97*

As two representative cases, Fe K-edge EXAFS spectra for $x = -1.0$ and $x = 0.2$ compositions have been plotted in Figs. 2(a) and 2(b), respectively, while the corresponding Fourier transform along with the respective best theoretical curves are shown in Figs. 2(c) and 2(d). The information about the local coordination around the absorber Fe, obtained from the fitting, is listed in Table II. The most important observation is that in all cases Fe ions have more Fe ions for neighbors than what is expected from the diffraction-based crystal structure (the quantity within the square brackets is the expected coordination from the refined crystal structure in Table I). For example, Fe located at the $4f$ site for $x = 0.2$ composition finds 0.38 Fe in the other site of the dimeric unit, while the expected coordination is only 0.06 from x-ray diffraction. So once again, the presence of microscopic Fe-rich regions is confirmed, which naturally predicts the complementary presence of Ru-rich regions, so that the overall nominal chemical composition is preserved. One interesting point is that the probability of finding two Fe ions in one Fe_2O_9 unit is found to be almost the same in each composition, strongly suggesting a very similar composition of the Fe-rich phase in each compound. Therefore, the only way the system could chemically organize itself is by decreasing (increasing) the volume fraction of the Fe-rich (Ru-rich) phase and decreasing the Ru oxidation state with increasing x. Such evolution of the local structure with chemical phase separation should result in a gradual change in electronic and magnetic properties with doping.

The $6H$ $BaRuO_3$ is metallic and Pauli paramagnetic in nature [29], and the other end member of the series, $BaFeO_{3-\delta}$ (oxygen vacancy exists due to only a partial tetravalent state of the Fe cation), is highly insulating [30]. So any solid solution between these is expected to exhibit a metal-insulator transition at some critical doping concentration x_c. Such doping- controlled (at the B site of ABO_3) metal-insulator transition (MIT) has previously been observed in numerous systems, e.g., $LaNi_{1-x}M_xO_3$ (with M = Mn, Co, Fe) [31], $LaTi_{1-x}V_xO_3$ [32], $BaCo_{1-x}Ni_xS_2$ [33], $SrRu_{1-x}Ti_xO_3$ [34], $Sr_2Ru_{1-x}Ti_xO_4$ [35], $SrMn_{1-x}Fe_xO_3$ [36], to name a few.

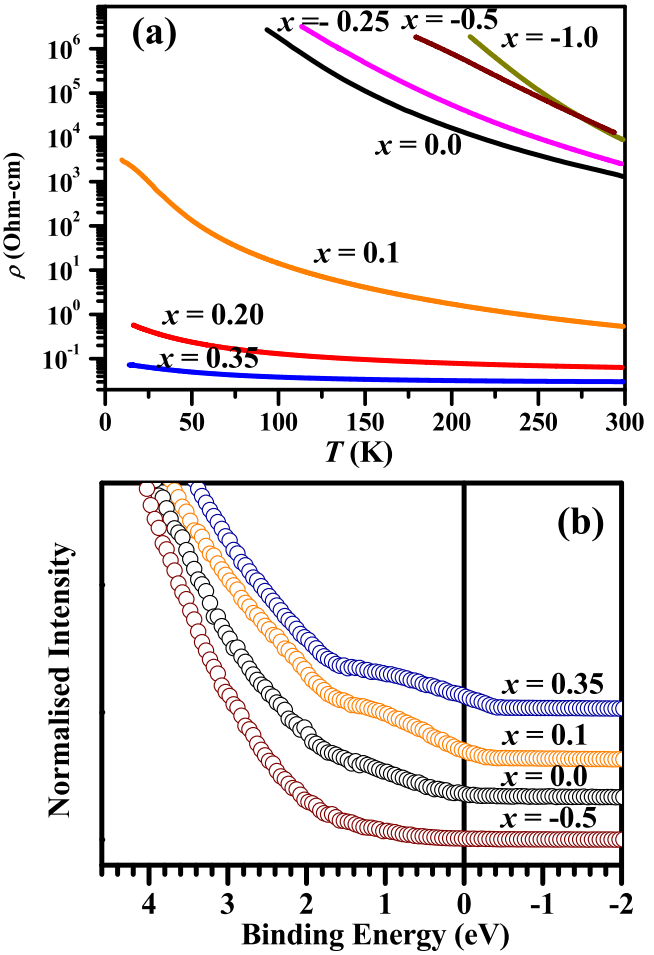

FIG. 3. (a) ρ is plotted as a function of T for the $Ba_3Fe_{1-x}Ru_{2+x}O_9$ series. (b) He I UPS valence band spectra for several members of the series. Data have been shifted vertically for visual clarity.

However, the presence of significant chemical inhomogeneity in the present series of compounds introduces additional complexity. The expected electronic and magnetic structures were investigated using the plane-wave pseudopotential implementation of density-functional theory and projector augmented-wave potentials [37] in the VASP code [38] for $x = 0.5$ and $x = -0.5$, considering the phase separation described above [Figs. S3(a) and S3(b)]. The details of the calculations and results are presented in the Supplementary Material. All possible magnetic configurations, considering ferromagnetic and antiferromagnetic interactions, were examined within these 30-atom supercells. The ferromagnetic (ferrimagnetic) state for $x = 0.5$ (-0.5) is found to be lower in energy by -22 meV/f.u. $(-50$ meV/f.u.) compared to the next low-lying spin configuration. The total density of states (DOS), the sum of Fe and Ru partial d DOSs [plotted in Fig. S3(c)], emphasizes the metallic (insulating) nature of the $x = 0.5$ $(x = -0.5)$ phase. A decrease in total magnetic moment can also be anticipated with the increase of Fe content from these calculations.

Electrical resistivities ρ of several members of the present series are plotted as a function of T in Fig. 3(a) on a logarithmic scale. The plot shows that the ρ value at room temperature increases continuously with the increase in Fe content with a discrete jump in between $x = 0.1$ and $x = 0.0$, which is possibly indicative of a MIT. The difference in ρ between the two end compositions of the series ($x = -1.0$ and $x = 0.35$) is very large, and the members with $x \leqslant 0$ have very high resistivities and exhibit clear insulating behavior with decreasing T. The weak semiconductorlike behavior for $x \geqslant 0.2$ compounds in dc transport measurement appears due to the polycrystalline grain boundary contribution as intrinsic metallic behavior has been verified by valence-band spectra measurement, shown in Fig. 3(b). Overall, we do find a distinct MIT in this series of compounds, with the critical composition x_c for MIT being between 0.0 and 0.1.

Next, we show the valence-band spectra near the Fermi level for $x = -0.5$, 0.0, 0.1, and 0.35 compounds, recorded using He I ($h\nu = 21.22$ eV), normalized at 4 eV from the Fermi cutoff, in Fig. 3(b). The normalization was made taking into account the negligible contribution of Fe and Ru calculated from their partial DOSs [Fig. S3(c)] at around 4 eV from the Fermi level where the only contribution comes from O $2p$, the only invariant contribution throughout the series. Also, it can be inferred from the band structure calculation [Fig. S3(c)] that the states at the Fermi level are mainly contributed by Ru d states. Now, the presence of the finite density of states at E_F for $x = 0.35$ confirms its metallic behavior. However, with increasing Fe concentration the DOS at E_F decreases gradually, and for the $x = -0.5$ composition, there are indeed no states at E_F mimicking its insulating nature. If this metal-insulator transition were the Mott-Hubbard type like Ti-doped Sr_2RuO_4 [35], then the disappearance of intensities at E_F would have been very abrupt at a certain value of x. On the contrary, the rather slow, continuous disappearance of DOS near E_F here suggests that the present MIT is of percolative type. It is already apparent from the EXAFS that all the compounds in the series are divided into inhomogeneous Fe-rich and Ru-rich regions, having varying volume fractions as a function of x. So for low-Fe-content compounds, the Ru-rich metallic patches, engulfing the isolated Fe-rich clusters, are expected to maintain conduction channels, and the systems behave as metals. The situation gradually reverses as the Fe content increases; the isolated Fe clusters began to percolate and finally encapsulate the metallic Ru-rich islands, cutting off the conduction channel, and the system shows a jump in the resistivity around $x = 0.0$ [Fig. 3(a)]. Thus, our photoemission spectroscopic results convincingly confirm the percolation-driven MIT in the $Ba_3Fe_{1-x}Ru_{2+x}O_9$ series of compounds.

After confirming the presence of local chemical clustering and a percolative-type MIT, let's discuss how the magnetic properties vary as a function of x. The field-cooled (FC) and zero-field-cooled (ZFC) magnetization curves from all the samples recorded with 100-Oe field are plotted in Fig. 4 as a function of temperature. The ZFC and FC data were taken during heating to room temperature after cooling the sample from 300 to 2 K in the absence (presence) of magnetic field for ZFC (FC) data acquisition. For the most Fe deficient sample, $x = 0.35$, FC and ZFC start to diverge from 35 K. Both FC and ZFC magnetization continue to increase with decreasing temperature, and the ZFC curve exhibits two peaks around 26 and 12 K. For $x = 0.2$ onwards, the bifurcation between the FC and ZFC magnetization curves progressively starts to appear

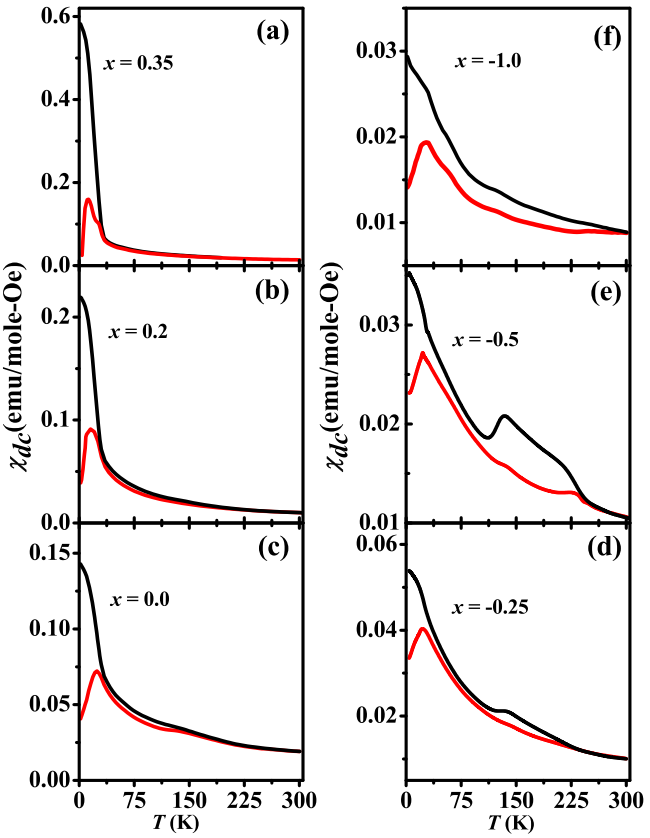

FIG. 4. Field-cooled and zero-field-cooled magnetization vs T measured with $H = 100$ Oe. The FC-ZFC data for $x = 0.0$ have been taken from Ref. [9].

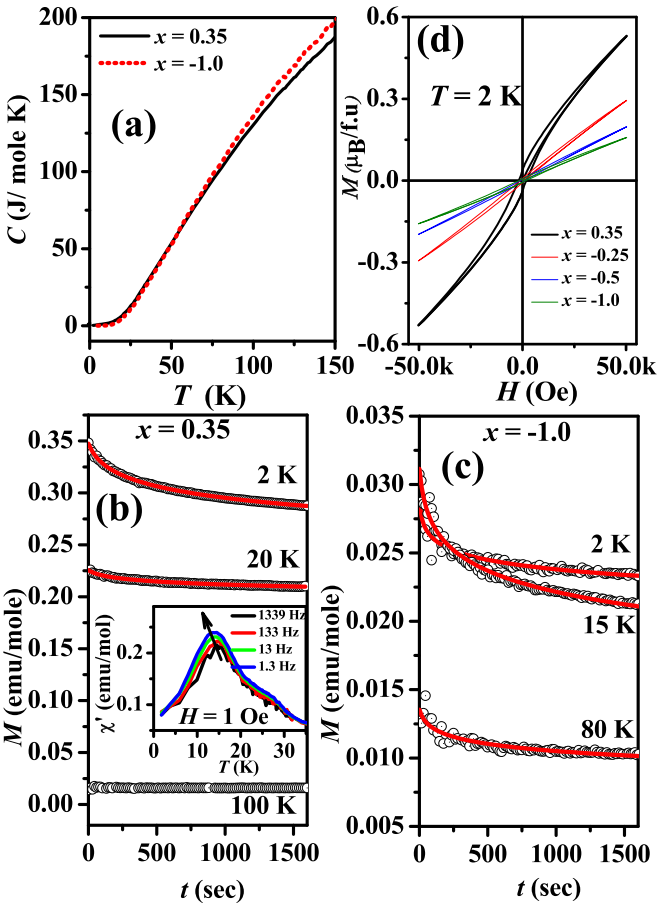

FIG. 5. (a) Variation of heat capacity C with temperature T. The variation of IRM with time t at different temperatures for (b) $x = 0.35$ and (c) $x = -1.0$. These relaxations can be described (red solid lines) by the relation $M_{IRM} = M_0 - S\ln(1 + t/t_0)$, a very general characteristic of materials with hysteretic magnetization and/or spin glass [9,40,41]. The real part of ac susceptibility for $x = 0.35$ is plotted as a function of T in the inset in (b). (d) M vs H measured at 2 K for different compositions.

at higher and higher temperatures with prominent additional magnetization features, but the magnetization features at low temperature continues to remain very similar, although there is a regular drop in magnetization values with increasing Fe doping. For the $x = -1.0$ composition, FC-ZFC curves start to diverge even above room temperature, while the low-temperature magnetization value is nearly a factor of 20 lower than that of the $x = 0.35$ member. Here it can be assumed that the low-temperature magnetization features appear from isolated $6H$ Fe-rich regions which remain visible throughout the series but with decreasing dominance with increasing Fe content. Now, it is expected that with increasing Fe content, the isolated Fe-rich clusters would progressively start to percolate and interact antiferromagnetically with many Fe^{3+}-O-Fe^{3+} 180° connections [39], thereby decreasing the low-temperature contribution from individual clusters and, in exchange, building up additional wide magnetic responses at higher temperatures. The spatially inhomogeneous percolation paths should produce many magnetically connected patches of various sizes with varying magnetic transition temperatures, which is manifested in the wide FC-ZFC divergent features at higher temperatures.

In order to check whether the observed magnetic transitions have long-range nature or not, the heat capacity C was measured for two extreme end members of the series and is shown in Fig. 5(a) as a function of T. The absence of any feature in C confirms that none of the magnetic transitions have long-range coherent magnetic order [9]. To further understand the nature of the magnetic transition(s) observed at low temperature, ac susceptibility was measured as a function of T for $x = 0.0$ and the two end members of the series. Unfortunately, the data were too noisy for $x = 0.0$ and $x = -1.0$ due to a very small moment. The real part of the ac susceptibility from $x = 0.35$ [inset in Fig. 5(b)] shows a continuously shifting peak near 15 K with the frequency of measurement, which confirms that the low-temperature signal from the isolated clusters is of spin-glass character. The low-temperature transitions for the other members are also of similar metastable nature. In order to further confirm this point, isothermal remanent magnetization (IRM) measurements were carried out. For this measurement, the sample was cooled from 300 K in zero field to the measuring temperature, a 5 kOe field was applied for 5 min, and then M was noted as a function of time t immediately after the field was switched off. The results are shown in Figs. 5(b) and 5(c). As expected for a spin glass, M_{IRM} undergoes a slow decay with time at 2 and 20 K for the $x = 0.35$ composition. Similar behaviors of M_{IRM} were

observed for $x = -1.0$ at $T = 1.8$ and 15 K, indicative of a glassy behavior. However, the IRM at 100 K for $x = 0.35$ is independent of time and is almost negligible compared to the IRM at 2 K, contrary to the high-temperature IRM behavior of $x = 0.0$ [9]. However, this is fully consistent with the observation that there are no magnetic anomalies at the high-temperature $M(T)$ curve for $x = 0.35$ as the probability of magnetic percolation of isolated Fe-rich clusters is low in this case. On the other hand, IRM for $x = -1.0$ at 80 K shows a clear relaxation behavior similar to that at 2 K due to the presence of a huge number of magnetically connected Fe-rich regions which start to order (again a glasslike order as individual spin-glass clusters start to interact and create wide percolative patches) even above room temperature. M vs H loops, measured after zero field cooling to 2 K for a few members of the series, are shown in Fig. 5(d). For all of them, $M(H)$ curves show clear hysteresis loops with coercivity between 1000 and 2000 Oe but without any signature of saturation until the highest field of measurement, typical of spin-glass order. The magnetization observed at the maximum field of measurement (50 kOe) expectedly decreases while going from $x = 0.35$ to $x = -1.0$ as the contribution from individual, isolated $6H$ Fe-rich clusters decreases.

IV. CONCLUSION

$Ba_3FeRu_2O_9$ is a special member with respect to other members of the $Ba_3MRu_2O_9$ family, where the possibility of Fe/Ru site disorder gives rise to many competing magnetic interactions and an extreme microscopic phase separation. Our results show that if $BaRuO_3$, a paramagnetic metal, is progressively doped with Fe, microscopic phase separation becomes unavoidable, and the system undergoes a MIT and a magnetic changeover through percolative paths.

ACKNOWLEDGMENTS

P.A. thanks CSIR, India, for a fellowship. S.R. thanks Indo-Italian POC for support to carry out experiments in Elettra, Italy. We thank D. D. Sarma for useful discussions.

[1] M. Imada, A. Fujimori, and Y. Tokura, Rev. Mod. Phys. **70**, 1039 (1998).
[2] Y. Tokura, Rep. Prog. Phys. **69**, 797 (2006).
[3] N. P. Armitage, P. Fournier, and R. L. Greene, Rev. Mod. Phys. **82**, 2421 (2010).
[4] S. J. May, P. J. Ryan, J. L. Robertson, J. W. Kim, T. S. Santos, E. Karapetrova, J. L. Zarestky, X. Zhai, S. G. E. te Velthuis, J. N. Eckstein, S. D. Bader, and A. Bhattacharya, Nat. Mater. **8**, 892 (2009).
[5] C. Meneghini, S. Ray, F. Liscio, F. Bardelli, S. Mobilio, and D. D. Sarma, Phys. Rev. Lett. **103**, 046403 (2009).
[6] T. Chakraborty, S. Baidya, C. Meneghini, T. Saha-Dasgupta, G. Veronesi, M. Merlini, H. Yokota, M. Itoh, S. Majumdar, and S. Ray, Phys. Rev. B **90**, 235147 (2014); T. Chakraborty, C. Meneghini, G. Aquilanti, and S. Ray, J. Appl. Phys. **114**, 223911 (2013); J. Phys. Condens. Matter **25**, 236002 (2013).
[7] S. Jana, V. Singh, S. D. Kaushik, C. Meneghini, P. Pal, R. Knut, O. Karis, I. Dasgupta, V. Siruguri, and S. Ray, Phys. Rev. B **82**, 180407(R) (2010); S. Jana, C. Meneghini, P. Sanyal, S. Sarkar, T. Saha-Dasgupta, O. Karis, and S. Ray, *ibid.* **86**, 054433 (2012); S. Jana, V. Singh, A. Nag, C. Meneghini, I. Dasgupta, G. Aquilanti, and S. Ray, *ibid.* **86**, 014203 (2012).
[8] J. T. Rijssenbeek, P. Matl, B. Batlogg, N. P. Ong, and R. J. Cava, Phys. Rev. B **58**, 10315 (1998).
[9] S. Middey, S. Ray, K. Mukherjee, P. L. Paulose, E. V. Sampathkumaran, C. Meneghini, S. D. Kaushik, V. Siruguri, K. Kovnir, and D. D. Sarma, Phys. Rev. B **83**, 144419 (2011).
[10] W. Miiller, M. Avdeev, Q. Zhou, A. J. Studer, B. J. Kennedy, G. J. Kearley, and C. D. Ling, Phys. Rev. B **84**, 220406(R) (2011).
[11] H. D. Zhou, A. Kiswandhi, Y. Barlas, J. S. Brooks, T. Siegrist, G. Li, L. Balicas, J. G. Cheng, and F. Rivadulla, Phys. Rev. B **85**, 041201(R) (2012).
[12] S. A. J. Kimber, M. S. Senn, S. Fratini, H. Wu, A. H. Hill, P. Manuel, J. P. Attfield, D. N. Argyriou, and P. F. Henry, Phys. Rev. Lett. **108**, 217205 (2012).
[13] P. Beran, S. A. Ivanov, P. Nordblad, S. Middey, A. Nag, D. D. Sarma, S. Ray, and R. Mathieu, J. Solid State Sci. **50**, 58 (2015).
[14] A. Nag, S. Middey, S. Bhowal, S.K. Panda, R. Mathieu, J. C. Orain, F. Bert, P. Mendels, P. G. Freeman, M. Mansson, H. M. Ronnow, M. Telling, P. K. Biswas, D. Sheptyakov, S. D. Kaushik, V. Siruguri, C. Meneghini, D. D. Sarma, I. Dasgupta, and S. Ray, Phys. Rev. Lett. **116**, 097205 (2016).
[15] J. T. Rijssenbeek, R. Jin, Yu. Zadorozhny, Y. Liu, B. Batlogg, and R. J. Cava, Phys. Rev. B **59**, 4561 (1999).
[16] N. Hayashi, T. Yamamoto, H. Kageyama, M. Nishi, Y. Watanabe, T. Kawakami, Y. Matsushita, A. Fujimori, and M. Takano, Angew. Chem. Int. Ed. **50**, 12547 (2011).
[17] T. Tsuyama, T. Matsuda, S. Chakraverty, J. Okamoto, E. Ikenaga, A. Tanaka, T. Mizokawa, H. Y. Hwang, Y. Tokura, and H. Wadati, Phys. Rev. B **91**, 115101 (2015).
[18] J. Rodríguez-Carvajal, Physica B (Amsterdam, Neth.) **192**, 55 (1993).
[19] A. Di Cicco, G. Aquilanti, M. Minicucci, E. Principi, N. Novello, A. Cognigni, and L. Olivi, J. Phys. Conf. Ser. **190**, 012043 (2009).
[20] See Supplemental Material at http://link.aps.org/supplemental/10.1103/PhysRevB.94.184424 which includes Refs. [37,38] and the powder XRD pattern of $x = 0.35$, the XANES spectra demonstrating the oxidation state of Fe, the density functional theory (DFT) calculations and the corresponding figures.
[21] A. R. Denton and N. W. Ashcroft, Phys. Rev. A **43**, 3161 (1991).
[22] R. D. Shannon, Acta Crystallogr., Sect. A **32**, 751 (1976).
[23] Ionic radii of Fe^{3+}, Ru^{4+}, and Ru^{5+} are 0.645, 0.62, and 0.565 Å, respectively [22]. The average Shannon radii $r_{\text{eff}} = \frac{(1-x)r_{Fe}+(2+x)r_{Ru}}{3}$ are 0.605, 0.608, 0.61, 0.612, 0.614 for $x = -0.5, -0.25, 0.0, 0.2, 0.35$, respectively, considering Fe in a $+3$ state (confirmed by XAS measurements) and Ru having a mixed $+4/+5$ valency.
[24] K. E. Stitzer, M. D. Smith, W. R. Gemmill, and H. Z. Loye, J. Am. Chem. Soc. **124**, 13877 (2002).
[25] M. W. Lufaso and H. Z. Loye, Inorg. Chem. **44**, 9154 (2005).

[26] C. Menehgini, F. Bardelli, and S. Mobilio, Nucl. Instrum. Methods Phys. Res., Sect. B **285**, 153 (2012).
[27] J. J. Rehr and R. C. Albers, Rev. Mod. Phys. **72**, 621 (2000).
[28] Notice that while for single-scattering contributions their multiplicity corresponds to the average absorber coordination number, this is not true in the case of multiple scattering or dealing with complex chemical order as in this case.
[29] J. G. Zhao, L. X. Yang, Y. Yu, F. Y. Li, R. C. Yu, Z. Fang, L. C. Chen, and C. Q. Jin, J. Solid State Chem. **180**, 2816 (2006).
[30] J. Hombo, Y. Matsumoto, and T. Kawano, J. Solid State Chem. **84**, 138 (1990).
[31] P. Ganguly, N. Y. Vasanthacharya, C. N. R. Rao, and P. P. Edwards, J. Solid State Chem. **54**, 400 (1984).
[32] C. Eylem, Y. C. Hung, H. L. Ju, J. Y. Kim, D. C. Green, T. Vogt, J. A. Hriljac, B. W. Eichhorn, R. L. Greene, and L. Salamanca-Riba, Chem. Mater. **8**, 418 (1996).
[33] S. R. Krishnakumar, T. Saha-Dasgupta, N. Shanthi, P. Mahadevan, and D. D. Sarma, Phys. Rev. B **63**, 045111 (2001).
[34] K. W. Kim, J. S. Lee, T. W. Noh, S. R. Lee, and K. Char, Phys. Rev. B **71**, 125104 (2005).
[35] S. Ray, D. D. Sarma, and R. Vijayaraghavan, Phys. Rev. B **73**, 165105 (2006).
[36] D. H. Kim, H. J. Lee, B. Dabrowski, S. Kolesnik, J. Lee, B. Kim, B. I. Min, and J. S. Kang, Phys. Rev. B **81**, 073101 (2010).
[37] P. E. Blochl, Phys. Rev. B **50**, 17953 (1994); G. Kresse and D. Joubert, *ibid.* **59**, 1758 (1999).
[38] G. Kresse and J. Furthmüller, Phys. Rev. B **54**, 11169 (1996); Comput. Mater. Sci. **6**, 15 (1996).
[39] J. B. Goodenough, Phys. Rev. **100**, 564 (1955); J. Kanomari, J. Phys. Chem. Solids **10**, 87 (1959).
[40] S. Majumdar, E. V. Sampathkumaran, D. Eckert, A. Handstein, K. H. Müller, S. R. Saha, H. Sugawara, and H. Sato, J. Phys. Condens. Matter **11**, L329 (1999).
[41] D. X. Li, S. Nimori, Y. Shiokawa, Y. Haga, E. Yamamoto, and Y. Onuki, Solid State Commun. **120**, 227 (2001).